Reovirus infection is regulated by NPC1 and endosomal cholesterol homeostasis

Paula Ortega,[a,b,c,d] Gwen Taylor,[c,d] Rohit K. Jangra,[e,†] Raquel Tenorio,[a] Isabel Fernández de Castro,[a] Bernardo A. Mainou,[f,††] Robert C. Orchard,[g] Craig B. Wilen,[h] Pamela A. Brigleb,[c,i] Jorna Sojati,[c,i] Kartik Chandran,[e] Cristina Risco,[a,*] and Terence S. Dermody,[c,d,i,*]

[a]Cell Structure Laboratory, National Center for Biotechnology, CNB-CSIC, campus UAM, Cantoblanco, 28049 Madrid, Spain

[b]PhD Program in Molecular Biosciences, Autonoma de Madrid University, 28049 Madrid, Spain

[c]Department of Pediatrics, University of Pittsburgh School of Medicine, Pittsburgh, Pennsylvania, USA

[d]Institute of Infection, Inflammation, and Immunity, UPMC Children's Hospital of Pittsburgh, Pittsburgh, Pennsylvania, USA

[e]Department of Microbiology and Immunology, Albert Einstein College of Medicine, Bronx, New York, USA

[f]Department of Pediatrics, Vanderbilt University School of Medicine, Nashville, Tennessee, USA

[g]Department of Immunology, University of Texas Southwestern Medical Center, Dallas, Texas, USA

[h]Departments of Laboratory Medicine and Immunobiology, Yale University School of Medicine, New Haven, Connecticut, USA

[i]Department of Microbiology and Molecular Genetics, University of Pittsburgh School of Medicine, Pittsburgh, Pennsylvania, USA

[†]Current address: Department of Microbiology and Immunology, Louisiana State University Shreveport, Shreveport, Louisiana, USA

[††]Current address: Centers for Disease Control and Prevention, Atlanta, Georgia, USA

[*]Corresponding authors: crisco@cnb.csic.es and terence.dermody@chp.edu

Running title: Reovirus infection is regulated by NPC1 and endosomal cholesterol homeostasis

ABSTRACT Cholesterol homeostasis is required for the replication of many viruses, including Ebola virus, hepatitis C virus, and human immunodeficiency virus-1. Niemann-Pick C1 (NPC1) is an endosomal-lysosomal membrane protein involved in cholesterol trafficking from late endosomes and lysosomes to the endoplasmic reticulum. We identified NPC1 in CRISPR and RNA interference screens as a putative host factor for infection by mammalian orthoreovirus (reovirus). Following internalization via clathrin-mediated endocytosis, the reovirus outer capsid is proteolytically removed, the endosomal membrane is disrupted, and the viral core is released into the cytoplasm where viral transcription, genome replication, and assembly take place. We found that reovirus infection is significantly impaired in cells lacking NPC1, but infection is restored by treatment of cells with hydroxypropyl-β-cyclodextrin, which binds and solubilizes cholesterol. Absence of NPC1 did not dampen infection by infectious subvirion particles, which are reovirus disassembly intermediates that bypass the endocytic pathway for infection of target cells. NPC1 is not required for reovirus attachment to the plasma membrane, internalization into cells, or uncoating within endosomes. Instead, NPC1 is required for delivery of transcriptionally active reovirus core particles into the cytoplasm. These findings suggest that cholesterol homeostasis, ensured by NPC1 transport activity, is required for reovirus penetration into the cytoplasm, pointing to a new function for NPC1 and cholesterol homeostasis in viral infection.

IMPORTANCE Genetic screens are useful strategies to identify host factors required for viral infection. NPC1 was identified in independent CRISPR and RNA interference screens as a putative host factor required for reovirus replication. We discovered that NPC1-mediated cholesterol transport is dispensable for reovirus attachment, internalization, or disassembly but required for penetration of the viral disassembly intermediate from late endosomes into the cytoplasm. These findings pinpoint an essential function for cholesterol in the entry of reovirus and raise the possibility that cholesterol homeostasis regulates the entry of other viruses that penetrate late endosomes to initiate replication.

INTRODUCTION

Viral replication is dependent on cellular proteins and pathways for entry, transport, and release of the viral genome to sites of replication in the cell. Viral attachment to host cells occurs by interactions with cell-surface proteins, lipids, and carbohydrate moieties at the plasma membrane and often triggers virus uptake by receptor-mediated endocytosis (1-7). Viruses that traverse through endosomes must escape the endosomal compartment and release their genomes at sites of replication to initiate productive infection. Enveloped viruses generally accomplish endosomal escape using mechanisms involving receptor- or pH-mediated fusion of the viral envelope and endosomal membrane (6, 8-10). In contrast, nonenveloped viruses penetrate endosomal membranes by establishing small membrane pores or large membrane disruptions (9, 11-13). While both enveloped and nonenveloped viruses depend on conformational changes of viral structural proteins to escape endosomes, mechanisms underlying nonenveloped virus membrane penetration are not well understood (6).

Mammalian orthoreoviruses (reoviruses) are nonenveloped icosahedral viruses that infect a broad range of mammalian hosts. Reovirus infections are usually asymptomatic in humans, but these viruses have been implicated in development of celiac disease (14). Reovirus virions include two protein shells, the outer capsid, composed primarily of μ1-σ3 heterohexamers, and core (15-17). Within the core, 10 segments of double-stranded (ds) RNA are packaged, distributed by size into three large (L), three medium (M), and four small (S) segments (17). Following receptor-mediated endocytosis, the reovirus outer capsid undergoes a series of conformational changes and disassembly events required for release of transcriptionally active cores into the cytoplasm (18, 19).

Within late endosomes, acid-dependent cathepsin proteases catalyze proteolysis of the viral outer-capsid protein σ3 and cleavage of the membrane-penetration protein μ1 to δ and φ, resulting in formation of metastable intermediates termed infectious subvirion particles (ISVPs) (20-24). Endosomal lipid composition induces ISVPs to undergo additional conformational changes resulting in exposure of hydrophobic domains of δ, release of pore-forming fragment μ1N, and formation of ISVP*s (25, 26). Release of μ1N during ISVP-to-ISVP* conversion leads to endosomal penetration and release of the viral core into the cytoplasm where infection progresses (27-31). Although some essential viral and host factors required for reovirus penetration of the endosome are known, the process is still not well understood.

In this study, we used RNA interference and CRISPR screens to discover that Niemann Pick C1 (NPC1), an endolysosomal transmembrane protein that mediates cholesterol egress from late endosomes for redistribution to cellular membranes (32-34), is required for reovirus infection. We found that genetic ablation of NPC1 in human brain microvascular endothelial cells (HBMECs) diminishes reovirus infection by virions but not by ISVPs, suggesting that NPC1 is required for steps that differ between virions and ISVPs. Treatment of NPC1-null HBMECs with hydroxypropyl-beta-cyclodextrin (HβCD), a macrocycle that binds and solubilizes cholesterol, restored infectivity by reovirus virions, suggesting that endosomal cholesterol homeostasis contributes to efficient reovirus entry. While NPC1 is not required for viral attachment to the plasma membrane, internalization, or uncoating within endosomes, we found that NPC1 is required for efficient release of reovirus cores from endosomes into the cytoplasm. Together, these findings suggest that cholesterol homeostasis, ensured by NPC1 cholesterol transport activity, is essential for reovirus cell entry and penetration into the cytoplasm.

RESULTS

CRISPR/Cas-9 and siRNA screens for host factors required for reovirus infection identify NPC1. To discover host factors required for reovirus infection, we conducted genome-wide CRISPR/Cas-9 and siRNA-based cell-survival screens. The CRISPR/Cas-9 screen was conducted using BV2 mouse microglial cells with the murine Asiago sgRNA library targeting over 20,000 genes. BV2 CRISPR cell libraries were infected with reovirus strains type 1 Lang (T1L) and type 3 Dearing (T3D) and cultured for nine days prior to isolation of genomic DNA (gDNA) from surviving cells and deep sequencing. STARS analysis was conducted to identify enriched CRISPR gRNAs within the surviving cell population (Fig. 1A and Table S1). The siRNA screen was conducted using HeLa S3 cells transfected with the ON-TARGET plus siRNA whole genome library targeting over 18,000 genes (35). Transfected cells were infected with reovirus strain T3SA+ and scored for viability using an ATP-dependent luminescence assay. T3SA+ contains nine genes from T1L and the S1 gene from strain T3C44-MA (36). T3SA+ binds all known reovirus receptors. Robust Z scores (median absolute deviation) were calculated for each sample (Fig. 1B and Table S2).

Key genes and pathways essential for reovirus replication were defined by comparing the CRISPR/Cas-9 and siRNA screen lists using STRING-db (Fig. 1C). In the CRISPR/Cas-9 screen, four functional pathways defined by Gene Ontology (GO) terms were common to both T1L and T3D, including sialic acid biosynthesis and metabolism (Fig. 1D). Sialic acid is a reovirus attachment factor, and genes involved in sialic acid biosynthesis and metabolism, including *Slc35a1*, are required for T3SA+ replication in BV2 cells (37). These data provide confidence that the target genes identified in the CRISPR/Cas-9 screen represent biologically significant candidates. We also compared KEGG pathways identified in the CRISPR/Cas-9 and siRNA screens to

increase the likelihood of significant gene targets. Ribosome and lysosome pathways were the only pathways common to both screens (Fig. 1E). Lysosomal genes include *Ctsl*, *Neu1*, and *Npc1*. *Ctsl* encodes cathepsin L, which is required for cleavage of the reovirus outer capsid to form ISVPs (22). *Neu1* encodes neuraminidase, a lysosomal sialidase that cleaves sialic acid linkages required for reovirus infectivity (38). *Npc1* encodes NPC1, a cholesterol transporter that resides in the limiting membrane of endosomes and lysosomes (33, 34).

Engineering and characterization of HBMECs with CRISPR-targeted Npc1. Based on the function of NPC1 in cell entry and replication of other viruses (39) and its identification in both our CRISPR and siRNA screens, we evaluated a potential role for NPC1 in reovirus replication. Human brain microvascular endothelial cells (HBMECs) are susceptible to reovirus infection (40) and amenable to CRISPR/Cas-9 gene editing (41). To facilitate these studies, we used CRISPR/Cas-9 gene editing to engineer a clonal HBMEC cell line lacking the *NPC1* gene (KO cells). The NPC1 KO cells were complemented by stable transfection of a functional NPC1 allele (KO+ cells).

The newly engineered NPC1 KO and KO+ cell lines were characterized for NPC1 expression and cholesterol distribution relative to wild-type (WT) HBMECs. Expression of NPC1 in WT, KO, and KO+ cells was determined by immunoblotting. As anticipated, NPC1 expression in KO cells was abrogated relative to WT and KO+ cells (Fig. S1A). There was an observable increase in NPC1 expression in KO+ cells compared with WT cells (Fig. S1B), but the difference was not statistically significant. In the absence of functional NPC1, cholesterol reorganizes from a homogeneous distribution to accumulate in endosomal compartments (32, 33). To define the distribution of cholesterol in NPC1-null HBMECs, we used fluorescent filipin III to label cholesterol in fixed cells and imaged cholesterol distribution using fluorescence

174 microscopy (Fig. S1C). As anticipated, cholesterol distribution was homogeneous in WT
175 (Fig. S1C, left) and KO+ cells (Fig. S1C, right). However, cholesterol accumulated
176 around the nucleus in KO cells (Fig. S1C, center) in a pattern consistent with the
177 distribution of endosomes (Fig. S1D), confirming the absence of functional NPC1. Thus,
178 KO cells display the expected phenotype of altered cholesterol distribution when NPC1-
179 dependent cholesterol transport is disrupted. Furthermore, complementing NPC1
180 expression in KO cells restores the normal distribution of cholesterol, demonstrating
181 that the observed phenotype is specific for NPC1 expression.

182 **Reovirus infection by virions but not by ISVPs is impaired in NPC1 KO**
183 **cells.** ISVPs prepared by treatment of virions *in vitro* with intestinal or endosomal
184 proteases bind to reovirus receptors and enter target cells by direct penetration of the
185 plasma membrane and bypass requirements for internalization into the endocytic
186 compartment and acid-dependent proteolysis (21, 22, 42). To determine whether NPC1
187 is required for reovirus replication, and further whether NPC1 mediates a step in the
188 infectious cycle that differs between virions and ISVPs, we adsorbed WT, KO, and KO+
189 cells with reovirus strain T1L M1 P208S virions or ISVPs. Reovirus T1L M1-P208S
190 contains a point mutation in the M1 gene that causes viral factories to have a globular
191 morphology similar to the morphology of factories formed by reovirus T3D (43), which
192 renders infected cells easier to detect. Infected cells were visualized by
193 immunofluorescence (IF) staining for reovirus antigen at 18 h post-adsorption (Fig. 2).
194 Following adsorption with reovirus virions, the number of infected KO cells was reduced
195 by approximately 50% relative to infected WT and KO+ cells (Fig. 2A). A similar
196 reduction in the number of infected KO cells relative to WT and KO+ cells was observed
197 when WT, KO, and KO+ cells were adsorbed with T1L, T3D, and T3SA+ virions, the
198 reovirus strains used in the CRISPR/Cas9 and siRNA screens (Fig. S2). In contrast, no

significant differences in numbers of infected cells were observed following adsorption of WT, KO, and KO+ cells with ISVPs (Fig. 2B). Viral progeny production and release was determined by quantifying viral titers in cell lysates and supernatants at 0, 24, and 48 h following adsorption of WT, KO, and KO+ cells with virions or ISVPs. Following infection by virions, viral titers in lysates and supernatants of KO cells were 10- to 100-fold less than those in WT and KO+ cells (Fig. 2C and E). In contrast, following infection by ISVPs, viral titers in lysates and supernatants of all three cell types were comparable (Fig. 2D and F). Together, these results suggest that NPC1 is required for reovirus infection and functions at a step in the infectious cycle that differs between virions and ISVPs.

NPC1 is not required for reovirus attachment, internalization, or uncoating. Reovirus entry can be divided into four main stages: viral binding to cell-surface receptors, viral internalization by endocytosis, proteolytic removal of the viral outer capsid, and penetration of the core from late endosomes into the cytosol (19). We characterized NPC1 KO cells for the capacity to support each step of the reovirus entry pathway to define the function of NPC1 in reovirus infection. To determine whether NPC1 is required for reovirus attachment to target cells we quantified viral binding using flow cytometry. The quantity of virus bound to the surface of all three cell types was comparable, and no statistically significant differences were observed (Fig. 3A). These data suggest that reovirus attachment to cells is not dependent on expression of NPC1.

To determine whether NPC1 is required for reovirus to access the endocytic pathway of target cells, WT, KO, and KO+ cells were adsorbed with fluorescently-labeled reovirus particles and monitored for reovirus uptake using live-cell imaging. We found that kinetics of reovirus internalization into WT, KO, and KO+ cells were comparable. High-magnification videos (Videos 1, 2, and 3) along with static images

obtained at different intervals (Fig. 3B) demonstrate that attached reovirus particles internalize slowly in the first ~ 0 - 10 min post-adsorption. During this time, reovirus particles remain in the periphery, with a few particles coalescing to form large fluorescent puncta. Convergence of immunofluorescent signals suggests co-transport of multiple viral particles in the same endocytic compartment, similar to that observed during reovirus entry into neurons (44). After ~ 15 min post-adsorption, there was rapid recruitment of almost every fluorescent puncta to the perinuclear region.

To more precisely define the movement of reovirus virions during entry, we analyzed the trajectories of individual fluorescent virions in Videos 1, 2, and 3 over 36 min using the Spot detector plugin function from Icy software. Trajectory colors change over time in which each color corresponds to an interval of ~ 7.5 min in the time-lapse videos (Videos 4, 5, and 6). Analysis of the time-dependent trajectories confirms observations made in the live-imaging videos. Video-microscopic analysis demonstrates that reovirus virions are internalized rapidly into HBMECs and that virion uptake into the endocytic pathway is not impaired in the absence of NPC1.

Following internalization of reovirus virions, acid-dependent cathepsin proteases in late endosomes catalyze disassembly. During disassembly, proteolytic cleavage of the outermost capsid protein, σ3, exposes the membrane-penetration protein, μ1, which is subsequently cleaved to form a variety of intermediates that lead to penetration of the core particle into the cytoplasm (20-24, 27-30). Cells lacking NPC1 have increased endosomal pH and decreased cathepsin activity (45), which could impair reovirus uncoating. To determine whether NPC1 is required for reovirus disassembly, we defined the kinetics of reovirus outer-capsid proteolysis by following the formation of the δ cleavage fragment of the μ1 protein in WT, KO, and KO+ cells. Cells were adsorbed with reovirus virions, and viral proteins in cell lysates were visualized by immunoblotting

at 0, 1, 2, and 3 h post-adsorption using a reovirus-specific antiserum. No significant differences in the kinetics of μ1 proteolysis were observed, with an initial δ cleavage product detected 2 h after adsorption in WT, KO, and KO+ cells (Fig. 3C). These data suggest that the cathepsins that catalyze reovirus disassembly are not impaired in NPC1 KO HBMECs. Collectively, these results demonstrate that NPC1 is not required for reovirus receptor binding, internalization, or disassembly.

Escape of reovirus cores from endosomes is impaired in cells lacking NPC1. To determine whether NPC1 is required for escape of reovirus cores into the cytoplasm following disassembly in the endocytic compartment, we imaged cores in fixed cells by IF. Cells were adsorbed with fluorescently labeled reovirus virions and incubated in the presence of cycloheximide for 8 h post-adsorption to inhibit synthesis of new viral proteins and thus ensure detection of proteins from infecting viral particles. Cells were stained with a CD-63-specific antibody to label endosomes and an antiserum specific for reovirus cores and imaged using confocal microscopy. Small puncta consistent with reovirus cores were observed in WT and KO+ cells, while in KO cells, cores appeared to accumulate in larger puncta corresponding to endosomes (Fig. 4A). The distribution of virions, cores, and endosomes was determined to quantify the extent of colocalization. The results demonstrate a strong colocalization of cores and endosomes in KO cells (Manders coefficient [Mc]: ~ 0.7), while there was much less colocalization of cores and endosomes in WT and KO+ cells (Mc: ~ 0.3) (Fig. 4B). Colocalization of virions and cores also was more frequent in KO cells (Mc: ~ 0.45) cells than in WT (Mc: ~0.15) or KO+ (Mc: ~0.2) cells, whereas colocalization of virions and endosomes was comparable in all cell types (Mc: ~ 0.6). These data suggest that escape of cores from endosomes is less efficient in the absence of NPC1.

To complement the imagining experiments, we quantified newly synthesized viral s4 mRNA using RT-qPCR. WT, KO, and KO+ cells were adsorbed with reovirus, RNA was isolated, and s4 transcripts were quantified at 0, 6, 12, and 24 h post-adsorption. We observed a statistically significant increase in total s4 RNA in WT and KO+ cells at 12 and 24 h post-adsorption relative to KO cells (Fig. 5). Together, these results suggest that NPC1 is required for release of transcriptionally active reovirus cores from endosomes into the cytoplasm.

Cholesterol homeostasis is required for reovirus entry. We thought it possible that NPC1 could serve as an endosomal receptor for reovirus and interact with one or more viral capsid proteins to enable core delivery into the cytoplasm, analogous to the function of NPC1 in Ebola virus infection (46, 47). Alternatively, NPC1 might be required to maintain an endosomal environment with appropriate cholesterol levels to allow cores to penetrate endosomes. To distinguish between these possibilities, we tested whether hydroxypropyl-β-cyclodextrin (HβCD), a cyclic oligosaccharide that triggers cholesterol release from the endo-lysosomal compartment (48, 49) and has shown efficacy in the treatment of the Niemann Pick type C disease (50, 51), for the capacity to overcome the effects of NPC1 deficiency on reovirus infection. To determine whether HβCD treatment redistributes cholesterol from endosomal membranes to a homogeneous distribution in the absence of NPC1, NPC1 KO HBMECs were treated with 1 mM HβCD, a non-toxic concentration (Fig. S3A), or PBS for 48 h prior to staining for the filipin III complex. Cells displaying cholesterol accumulation were distinguished from those with widely distributed cholesterol by quantifying the mean fluorescence intensity (MFI) of filipin III complex staining. Using this approach, an increase in MFI correlates with an increase in cholesterol accumulation. After HβCD treatment, KO cells displayed a significant redistribution of cholesterol, reducing its accumulation in

298 endosomes and enhancing its distribution broadly throughout the cell, correlating with a
299 statistically significant decrease in MFI (Fig. S3B,C). These data demonstrate that
300 HβCD treatment promotes cholesterol efflux in KO cells, resulting in a cholesterol-
301 distribution phenotype comparable to WT and KO+ cells (Fig. S3C).

302 Once we observed that HβCD treatment effectively redistributes cholesterol in
303 KO cells and, thus, functionally complements NPC1 deficiency, we tested whether the
304 reovirus entry defect in KO cells is due to the absence of NPC1 or impaired cholesterol
305 homeostasis. WT, KO, and KO+ cells were pre-treated with 1 mM HβCD or PBS for 24
306 h, adsorbed with reovirus virions or ISVPs, and scored for reovirus infection by
307 immunostaining. Remarkably, HβCD treatment rescued infection of KO cells by reovirus
308 virions (Fig. 6) but did not appreciably affect infection of WT or KO+ cells. HβCD
309 treatment also did not affect infection of WT, KO, or KO+ cells by ISVPs. These data
310 demonstrate that endosomal cholesterol homeostasis regulates reovirus entry by
311 enhancing penetration of the reovirus core particle into the cytoplasm.

DISCUSSION

In this study, we identified NPC1 as a putative host factor required for reovirus infection using genome-wide CRISPR/Cas9 and siRNA-based cell-survival screens. NPC1 is an endolysosomal cholesterol transporter that mediates cholesterol homeostasis (32-34). Disruption of NPC1 results in cholesterol accumulation in late endosomes (Sup. Fig. 2C) and leads to Niemann-Pick type C disease (NPCD), an autosomal-recessive neurodegenerative disorder (32). Early steps in reovirus infection, including receptor binding, acid-dependent proteolytic disassembly, and ISVP-to-ISVP* conversion have been well characterized (19). However, penetration of endosomal membranes and release of viral cores into the cytoplasm are poorly understood processes. We used CRISPR/Cas9 gene-targeted HBMECs lacking NPC1 expression to study the function of NPC1 in reovirus infection. We discovered that NPC1 is dispensable for viral binding to cell-surface receptors (Fig. 3A), internalization of viral particles (Fig. 3B), and disassembly of the viral outer capsid (Fig. 3C). However, NPC1 is required for efficient penetration of reovirus cores into the cytoplasm (Fig. 4). Treatment with HβCD reduces cholesterol accumulation in endosomes (Sup. Fig. 3B and 3C) and restores reovirus infectivity in NPC1 KO cells (Fig. 6). These findings suggest that regulation of cholesterol in endosomal compartments is essential for reovirus entry into host cells.

NPC1 is required for the replication of several enveloped viruses. The filoviruses Ebola virus and Marburg virus use NPC1 as an intracellular receptor (46, 47). NPC1 also functions in enveloped virus replication by maintaining cholesterol homeostasis. Disruption of cholesterol homeostasis by inhibiting NPC1 prevents entry and replication of dengue virus (52) and African swine fever virus (53) and impairs exosome-dependent release of hepatitis C virus (54). Additionally, NPC1 has been implicated in entry of quasi-enveloped forms of hepatitis A virus and hepatitis E virus (55, 56). However,

NPC1 had not been previously appreciated to function in the replication of a nonenveloped virus.

We found that reovirus binding, internalization, and uncoating do not require NPC1, suggesting that NPC1 does not function as an intracellular receptor for reovirus. Instead, we found that cholesterol accumulation in the endocytic pathway diminishes the efficiency of reovirus core release into the cytoplasm. Using confocal microscopy, we visualized and quantified the distribution of fluoresceinated reovirus virions, reovirus cores, and late endosomes in infected cells (Fig. 4). Reovirus cores accumulate in the lumen of late endosomes in KO cells (Fig. 4A), while virions distribute to endosomes comparably in KO, WT, and KO+ (Fig. 4B). These findings suggest that cores do not escape from endosomes efficiently in the absence of NPC1. RNA synthesis, which occurs in the cytoplasm following release of cores from late endosomes, also was reduced in KO cells relative to WT and KO+ cells (Fig. 5), providing evidence that core escape from endosomes is required for initiation of transcription. It is not apparent how cholesterol accumulation in KO cells blocks core release from late endosomes.

In NPCD, disruption of cholesterol homeostasis causes changes in lipid composition of endosomal membranes (57, 58), inverting the ratio of phosphatidyl choline (PC) and phosphatidyl ethanolamine (PE). The change in PC:PE ratio may alter mechanical properties of endosomal membranes by inhibiting intra-endosomal membrane dynamics to favor negative curvature (57, 59). Membrane composition and dynamics can influence viral entry. Negative membrane curvature induced by addition of PE or the action of interferon induced transmembrane protein 3 (IFITM3) impairs adenovirus protein VI-mediated membrane disruption (60) and enveloped virus fusion (61), respectively. Although clearly nonenveloped, reovirus entry also is inhibited by IFITM3 (62). Many nonenveloped viruses use membrane-modifying proteins with the

362 capacity to interact, destabilize, and disrupt membranes to mediate genome release
363 into the cytoplasm (12, 63). However, the role of specific lipids in these processes is not
364 well defined.

365 During reovirus entry, ISVP-to-ISVP* conversion leads to release of
366 myristoylated μ1N, which interacts with late endosomal membranes to facilitate release
367 of cores into the cytoplasm (20-24). PE and PC concentrations in liposomes influence
368 the efficiency of ISVP-to-ISVP* conversion (25). Therefore, it is possible that changes in
369 membrane fluidity, width, or curvature caused by inversion of endosomal membrane
370 PC:PE ratio in NPC1 KO cells impedes membrane insertion of μ1N or formation and
371 expansion of the penetration pore. Additionally, accumulation of cholesterol within the
372 endosomal compartment of NPC1 KO cells could limit recruitment of ISVP*s to
373 membrane-inserted μ1N and the subsequent penetration of reovirus cores. Within the
374 *Reoviridae* family, bluetongue virus (BTV) outer-capsid protein VP5 penetrates late
375 endosomal membranes enriched in phospholipid lysobisphosphatidic acid (LBPA),
376 which is dependent on the anionic charge and membrane fluidic properties of LBPA
377 (64). LBPA enriched late endosomes are also required for efficient rotavirus entry (65).
378 Our data demonstrating the importance of cholesterol homeostasis in reovirus entry
379 along with the role of LBPA in BTV and rotavirus entry suggest that lipid composition of
380 late endosomes influences nonenveloped virus entry and illuminate a potential new
381 target for antiviral therapy.

382 Our findings parallel those of a companion study indicating a function for WD
383 repeat-containing protein 81 (WDR81) in reovirus entry (66). WDR81 was identified in a
384 CRISPR/Cas9 cell-survival screen using mouse embryo fibroblasts and found to be
385 required for a step in reovirus entry that follows ISVP formation. WDR81 is required for
386 the maturation of late endosomes by modulating levels of phosphatidylinositol 3-

phosphate (67). These findings, coupled with our studies of NPC1, suggest that ISVPs formed in an altered endocytic compartment of cells lacking either WDR81 or NPC1 cannot launch replication, whereas ISVPs adsorbed to the surface of such cells can. We think that alterations in cholesterol distribution might govern this difference in ISVP behavior.

Cholesterol accumulation due to NPC1 dysfunction also can lead to alterations in the distribution of host proteins, such as annexin A2 (ANXA2), which was identified in our siRNA screen, and annexin A6 (ANXA6) (68). ANXA2 and ANXA6 are multifunctional proteins involved in endosomal trafficking, segregation of membrane lipids, and membrane curvature regulation through membrane-cytoskeleton rearrangements (69). Disruption of NPC1 leads to increased concentrations of ANXA2 and ANXA6 in late endosomes in response to cholesterol accumulation (70, 71). It is possible that cholesterol accumulation in cells lacking NPC1 similarly alters the distribution or function of WDR81. Thus, dysfunction of endosomal proteins in NPC1-null cells might alter potential interactions of μ1N or the reovirus core with specific lipid microdomains or proteins and inhibit core release.

Genetic screens are useful approaches to identify host factors required for viral replication and provide valuable information about virus-cell interactions (72, 73). However, genetic screens frequently yield long lists of potential candidates, many of which are false-positives. To increase the likelihood of identifying host factors required for reovirus replication, we compared gene lists obtained from independent genome-wide CRISPR/Cas9 and siRNA-based cell-survival screens. Only 28 genes in the CRISPR/Cas9 screens using strains T1L and T3D were identified in the siRNA screen using strain T3SA+, 19 of which are ribosomal genes (Fig. 1B, C). Of the nine non-ribosomal genes, several encode proteins required for reovirus entry, including those

involved in sialic acid biosynthesis and metabolism (*Nans* and *Neu*) (37, 38) and viral disassembly (*Ctsl*) (22).

Our findings indicate that NPC1, which was identified in both CRISPR/Cas9 and siRNA screens, is required for efficient release of reovirus cores into the cytoplasm by regulating cholesterol homeostasis. High-resolution studies showing the precise distribution of reovirus virions and cores within endosomes will be required to understand how NPC1 and cholesterol homeostasis regulate core release. These studies will allow us to answer the following new questions: Do cores interact with endosomal membranes in KO cells? Does cholesterol impede interactions of cores with membranes? Are other lipids or proteins required for core release? Our ongoing work to answer these questions will clarify the functional elements of the reovirus entry pathway and lead to new approaches to block the entry of viruses that depend on tightly regulated cholesterol distribution in the endocytic pathway.

MATERIALS AND METHODS

Cells and viruses

HBMECs were cultured in growth medium (RPMI 1640 (Gibco) supplemented to contain 10% fetal bovine serum (FBS; VWR 97068-085), 10% Nu Serum (Corning), 1% MEM-vitamins (Corning), 1% sodium pyruvate (Gibco), 1% MEM non-essential amino acids (Gibco), 1% L-glutamine (Gibco), 1% penicillin/streptomycin (Gibco), and 0.1% amphotericin B (Sigma)) or infection medium (growth medium containing 2% FBS). BV2 mouse microglial cells were cultured in BV2 maintenance medium (DMEM supplemented to contain 10% FBS, 1% penicillin/streptomycin, 1% sodium pyruvate, and 1% sodium bicarbonate) or selection medium (maintenance media supplemented with 4 μg/ml blasticidin (Thermo Fisher) and 2.5 μg/ml puromycin (Sigma-Aldrich)). HeLa cells were cultured in Dulbecco modified Eagle medium (Gibco) supplemented to contain 10% FBS, minimal essential medium nonessential amino acid solution (Gibco), 0.11 mg/mL of sodium pyruvate (Gibco), and 1% penicillin/ streptomycin, and 0.1% amphotericin B (Sigma). Spinner-adapted L929 cells (originally obtained from the Bernard Fields laboratory; ATCC CCL-1) were grown in either suspension or monolayers in Joklik's modified Eagle's minimal essential medium (US Biological; M3867) supplemented to contain 5% FBS, 2 mM L-glutamine, 100 units/ml penicillin, 100 μg/ml streptomycin, and 0.1% amphotericin B.

Reovirus strains T1L, T3D, T3SA+, and T1L M1-P208S, were prepared from laboratory stocks by plaque purification followed by 3 to 4 passages in L929 cells. T3SA+ contains nine genes from T1L and the S1 gene from T3C44-MA (36). T1L M1-P208S contains a point mutation in the M1 gene that causes viral factories to have a globular morphology similar to the morphology of factories formed by reovirus T3D (43)

and can be readily scored for infection. Virions were purified from infected L929 cell lysates using cesium chloride gradient centrifugation as described (74). Viral titers were determined by plaque assay using L929 cells (75) and expressed as plaque forming units per ml (PFU/ml). Reovirus particle concentration was estimated by spectral absorbance of purified virions at 260 nm (optical density at 260 nm [OD_{260}] of 1 = $2.1x10^{12}$ particles/ml) (76).

Fluorescent reovirus particles were prepared by diluting 6×10^{12} reovirus particles/ml in 50 mM sodium bicarbonate buffer and incubating with 20 μM Alexa Fluor™ 647 NHS Ester (Succinimidyl Ester) (Invitrogen, A37573) at room temperature (RT) for 90 min, protected from light (77). Labeled virions were dialyzed at 4°C overnight with 2-3 buffer exchanges to remove unreacted dye.

ISVPs were prepared by incubating 2×10^{12} purified reovirus particles with 200 μg/mL chymotrypsin (Sigma, C3142) at 37°C for 60 min (23). Digestion was terminated by the addition of PMSF to a final concentration of 2 mM. Virion-to-ISVP conversion was confirmed by SDS-PAGE and colloidal blue staining to assess the loss of σ3 and cleavage of μ1C to δ.

Antibodies and dyes

Primary antibodies used for indirect immunofluorescence include anti-CD63 (1:250) (Thermofisher, #10628D), reovirus-specific polyclonal rabbit antiserum (1:1000) (78), and T1L core-specific rabbit antiserum (1:250) provided by Max Nibert (79). Alexa Fluor conjugated secondary antibodies (Thermo Fisher, #A11034, #A11030) were used to visualize antigen. Nuclei were stained with 4′,6-diamidino-2-phenylindole (DAPI, Invitrogen, D3571). Primary antibodies used for immunoblotting include reovirus-specific polyclonal rabbit antiserum, NPC1-specific polyclonal rabbit antiserum (Abcam,

134113), and mouse GAPDH monoclonal antibody for protein loading controls (Sigma, G8795). Anti-mouse IRDye680RD and anti-rabbit IRDye800CW (Licor) secondary antibodies were used.

CRISPR Screen

The screen was conducted and transduction validated as described (80). BV2 cells were transduced with pXPR_101 lentivirus encoding Cas9 (Addgene; 52962) and propagated for 11 days with BV2 Maintenance Medium supplemented to contain blasticidin. These parental BV2 or BV2-Cas9 cells were transduced for 2 days with pXPR_011 expressing eGFP (Addgene; 59702) and a short guide RNA (sgRNA) targeting eGFP at a multiplicity of infection (MOI) of less than 1 PFU/cell. Cells were selected for 5 days with BV2 selection medium. The frequency of eGFP-expressing cells was quantified by flow cytometry.

The murine Asiago sgRNA CRISPR library contains six independent genome-wide pools, in which each pool contains unique sgRNAs targeting 20,077 mouse genes. Four pools of the Asiago library were transduced into 5×10^7 BV2 cells at an MOI of 0.2 PFU/cell to establish four BV2 libraries. Two days post-transduction, cells were transferred to BV2 Selection Medium and propagated for 5 additional days. For each experimental condition, 10^7 BV2 library cells expressing Cas9 and sgRNAs were seeded in duplicate into T175 tissue culture flasks (Greiner Bio-One). Cells were inoculated with Opti-MEM supplemented to contain PBS (mock) or reovirus strains T1L or T3D at an MOI of 100 PFU/cell. Cells were incubated at RT for 1 h, followed by the addition of 20 mL of DMEM supplemented to contain 10% FBS, 1% penicillin/streptomycin, 1% sodium pyruvate, and 1% sodium bicarbonate. After 2 days post-inoculation (dpi) (mock) or 9 dpi (T1L or T3D conditions), cells were harvested and

genomic DNA (gDNA) was isolated from surviving cells using a QIAmp DNA Mini Kit (QIAGEN) according to the manufacturer's instructions.

CRISPR screen sequencing and analysis

Illumina sequencing and STARS analyses were conducted as described (81). The gDNA was aliquoted into a 96-well plate (Greiner Bio-One) with up to 10 µg gDNA in 50 µL of total volume per well. A polymerase chain reaction (PCR) master mix containing ExTaq DNA polymerase (Clontech), ExTaq buffer (Clontech), dNTPs, P5 stagger primer, and water was prepared. PCR master mix (40 µL) and 10 µL of a barcoded primer were added to each well containing gDNA. Samples were amplified using the following protocol: 95°C for 1 min, followed by 28 cycles of 94°C for 50 s, 52.5°C for 30 s, and 72°C for 30 s, and ending with a final 72°C extension for 10 min. PCR product was purified using Agencourt AMPure XP SPRI beads (Beckman Coulter) according to the manufacturer's instructions. Samples were sequenced using a HiSeq 2000 (Illumina). Following deconvolution of the barcodes in the P7 primer, sgRNA sequences were mapped to a reference file of sgRNAs from the Asiago library. To account for the varying number of reads per condition, read counts per sgRNA were normalized to 10^7 total reads per sample. Normalized values were then log-2 transformed. sgRNAs that were not detected were arbitrarily assigned a read count of 1. sgRNA frequencies were analyzed using STARS software to produce a rank ordered score for each gene. This score correlated with the sgRNA candidates that were above 10% of the total sequenced sgRNAs. Genes scoring above this threshold in either of the two independent subpools and in at least two of the four independent genome-wide pools were assigned a STAR score. In addition to the STAR score, screen results were

compared using false discovery rate (FDR) analyses to monitor gene-specific signal versus background noise. Statistical values of independent replicates were averaged.

Whole genome siRNA screen and analysis

The whole genome siRNA screen was conducted as described (35) using HeLa S3 cells and the Dharmacon ON-TARGETplus® SMARTpool® human siRNA library (Thermo Scientific) and strain T3SA+.

Production of NPC1 KO and KO+ cell lines

HBMEC single-cell clones with ablation of the *NPC1* gene were engineered using CRISPR/Cas9-mediated gene editing as described (82) using an NPC1-specific gRNA (5′ GGCCTTGTCATTACTTGAGGGGG 3′, targeting nucleotides 768-790 of the human NPC1 mRNA). Single-cell clones were screened for the loss of NPC1 function by filipin III staining (82). Genotype of the selected NPC1 KO clones was confirmed by Sanger sequencing followed by amplification of the genomic DNA sequences flanking the gRNA target site using forward (5′ TCATAAACACACCAAACTTGGAATC 3′) and reverse (5′ TCCTGCGGCAGAGGTTTTC 3′) primers. Sequences of the NPC1 alleles were deconvoluted using CRISP-ID (83). To confirm the specificity of *Npc1* knockout, cells of a single clone were transduced with a retrovirus vector (pBabe-Puro) expressing human NPC1 as described (47).

Indirect immunofluorescence staining

Cells were fixed with 4% paraformaldehyde (PFA, Electron Microscopy Sciences, 15712-s) in $PBS^{-/-}$ at RT for 20 min, washed three times with $PBS^{-/-}$, and permeabilized and blocked with 0.1% Triton X-100 and 2% FBS in $PBS^{-/-}$ at RT for 20 min. Cells were

incubated sequentially with primary antibody, Alexa Fluor-conjugated secondary antibody, and DAPI diluted in $PBS^{-/-}$ containing 0.1% Triton X-100 and 2% FBS at RT for 30 to 60 min. For cholesterol labeling, fixed and permeabilized cells were incubated with 50 µg/ml filipin III (Sigma, SAE0088) diluted in $PBS^{-/-}$ for 30 min. Coverslips were mounted using Prolong-gold (Molecular Probes). Confocal images were captured using a Leica-SP8 laser scanning confocal microscope equipped with an HCX PL APO 63X/1.4 N.A oil objective and processed using Fiji/ImageJ software.

SDS-PAGE and Immunoblotting

Cells harvested for protein extraction were lysed in Radioimmunoprecipitation Assay buffer (*RIPA buffer*; Thermo Fisher) supplemented with 1X protease inhibitors (Thermo Fisher). Protein concentration was quantified by Bradford assay (Bio-Rad) following the manufacturer's protocol. Samples for SDS-PAGE were diluted in 5X Laemmli sample buffer (Bio-Rad) containing 10% β-mercaptoethanol and incubated at 95°C for 10 min. Samples for detection of NPC1 were incubated at 70°C for 10 min to prevent aggregation. Equal amounts of protein were electrophoresed in 10% or 4-20% Mini-Protean TGX gels (Bio-Rad). Following electrophoresis, proteins were transferred to nitrocellulose membranes (Bio-Rad) for immunoblotting. Nitrocellulose membranes were incubated with 5% nonfat milk in TBS (50 mM Tris-HCl, pH 7.6; 150 mM NaCl) with 0.1% Tween 20 (TBS-T) and sequentially incubated with primary and secondary antibodies diluted in TBS-T at RT for 1 h. Immunoblot images were captured using an Odyssey CLx imaging system (Li-Cor) and protein bands were quantified using the Image Studio Lite software. Protein expression levels were normalized to GAPDH loading controls.

Quantification of reovirus infectivity

In experiments comparing infectivity of reovirus in KO, KO+, and WT HBMECs, cells were adsorbed with 10,000 reovirus virions or 100 ISVPs diluted in Opti-MEM (Invitrogen) at 37°C for 1 h. Following adsorption, the inoculum was removed, and cells were incubated in infection medium for 18 h before fixing in ice-cold methanol. In experiments comparing reovirus infectivity in the presence or absence of HβCD, cells were treated with 1 mM HβCD or PBS for 24 h prior to adsorption with reovirus. Following adsorption, fresh 1 mM HβCD was added to the medium for 18 h before fixing in ice-cold methanol. Fixed cells were washed with $PBS^{-/-}$, blocked with 1% bovine serum albumin (BSA), and incubated sequentially with reovirus-specific polyclonal rabbit antiserum, Alexa Fluor 488-conjugated anti-rabbit antibody, and DAPI in $PBS^{-/-}$ containing 0.5% Triton X-100. Cells were imaged using a Lionheart FX automated imager (BioTek) equipped with a 20X air objective, taking four fields-of-view from duplicate samples. Images were processed and signals quantified using Gen5+ software (BioTek).

Viral binding

KO, KO+, and WT HBMECs were detached from tissue-culture plates using CellStripper dissociation reagent (Corning), quenched with HBMEC medium, and washed with $PBS^{-/-}$. Cells were resuspended in $PBS^{-/-}$ at 10^6 cells/ml and adsorbed with 10,000 Alexa Fluor 647-labeled reovirus virions/cell at 4°C for 1 h with agitation. After binding, cells were washed twice with $PBS^{-/-}$ and fixed with 1% paraformaldehyde (PFA) supplemented with propidium iodide to determine cell viability. Cells were analyzed using an LSRII flow cytometer (BD Bioscience). Results were quantified using FlowJo V10 software.

600

601 **Live microscopy of reovirus internalization**

602 KO, KO+, and WT HBMECs were plated on glass-bottom p35 plates and adsorbed with
603 10,000 Alexa 647-labeled reovirus virions/cell at 4°C for 45 min to synchronize
604 infection. The inoculum was removed and replaced with fresh Opti-MEM without
605 phenol-red medium supplemented with 2% FBS. Reovirus transport was imaged using
606 a Leica DMI6000B fluorescence microscope with an HCX PL APO 63X/1.30 Gly
607 objective. Fluorescence and brightfield images were collected from 0 to 40 min post
608 adsorption every ~ 25 sec.

609

610 **Tracking of reovirus transport**

611 Automated tracking of fluorescent reovirus particles in time-lapse images was
612 conducted using Icy bioimage analysis software. Regions of interest (ROI)
613 corresponding to the cell periphery were selected for tracking analysis using the Spot
614 Detector plugin (84). The scale of the object (reovirus cores) to be analyzed was set at
615 a size of ~7 pixels per spot, and the threshold sensitivity was set at 100. Parameters
616 describing transport dynamics were considered as both diffusive and directed for
617 running tracking analysis. Results are presented in colored time-dependent tracks.

618

619 **Quantification of reovirus cores**

620 KO, KO+, and WT HBMECs were adsorbed with 10,000 Alexa Fluor 647-labeled
621 reovirus virions at 37°C for 45 min. The inoculum was removed, and the cells were
622 incubated in infection medium containing 100 µg/ml of cycloheximide for 8 h. After
623 fixation, cells were permeabilized and stained with T1L core-specific rabbit polyclonal
624 serum and anti-CD63 antibody. Confocal images were captured using a Leica-SP8

laser scanning confocal microscope equipped with an HCX PL APO 63X/1.4 N.A oil objective and processed using Fiji/ImageJ software. Colocalization of fluorescent reovirus virions (cyan puncta), reovirus cores (green puncta), and late endosomes (red puncta) was analyzed to differentiate infecting virions from cores released into the cytoplasm.

RNA extraction and purification

Cells were lysed using TRIzol reagent (Invitrogen). RNA was extracted with chloroform and purified using a PureLink RNA minikit (Invitrogen) with DNase treatment according to the manufacturer's instructions.

S4 quantitative RT-PCR

Total S4 RNA was quantified using qScript XLT one-step RT-qPCR ToughMix, Low ROX (Quanta Bioscience) and T3D_S4_qPCR primers (Forward: GAAGCATTTGCCTCACCATAG, Reverse: GATCTGTCCAACTTGAGTGTATTG) according to the manufacturer's instructions. The following RT-qPCR cycling protocol was used: cDNA synthesis (50°C for 10 min), initial denaturation (95°C for 1 min), and 40 PCR cycles (95°C for 10 s followed by a data collection step at 60°C for 1 min). S4 cDNA was detected using a fluorogenic probe (5′-FAM [fluorescent fluorescein]-AGCGCGCAAGAGGGATGGGA-BHQ [black hole quencher]-1-3′; Biosearch Technologies).

Statistical analysis

All data were analyzed using Graphpad Prism 8. Figure legends specify the number of experimental repeats and the statistical test applied for each analysis. Differences were considered statistically significant when *P* values were less than 0.05.

ACKNOWLEDGEMENTS

We thank members of the Dermody and Risco laboratories for many useful discussions. We are grateful to the UPMC Children's Hospital of Pittsburgh Rangos Research Center Cell Imaging Core Laboratory for assistance with microscopy. Special thanks to Dr. Martin Sachse for expert advice and for critical review of the manuscript and to Drs. Sylvia Gutiérrez-Erlandsson and Ana Oña for assistance with confocal microscopy.

This work was supported in part by Public Health Service award R01 AI032539 (C.R. and T.S.D.) and the Heinz Endowments (T.S.D.) and grants BIO2015-68758-R and RTI2018-094445-B-100 from the Ministry of Science and Innovation of Spain (C.R.).

AUTHOR CONTRIBUTIONS

Conceived and designed experiments: POG, GT CR TSD. **Performed experiments**: POG GT RKJ BAM RCO CBW. **Analyzed data**: POG GT. **Contributed reagents/materials/analysis tools**: RKJ RCO CBW KC HWV. **Wrote original draft**: POG, GT TSD. **Reviewed and edited paper**: POG GT RKJ RT IF BAM RCO CBW PAB JS KC HWV CR TSD.

669 **REFERENCES**

670 1. Mercer J, Helenius A. Virus entry by macropinocytosis. Nat Cell Biol.
671 2009;11(5):510-20.

672 2. Mercer J, Schelhaas M, Helenius A. Virus entry by endocytosis. Annu Rev
673 Biochem. 2010;79:803-33.

674 3. Yamauchi Y, Helenius A. Virus entry at a glance. J Cell Sci. 2013;126(Pt
675 6):1289-95.

676 4. Smith AE, Helenius A. How viruses enter animal cells. Science.
677 2004;304(5668):237-42.

678 5. Tsai B. Penetration of nonenveloped viruses into the cytoplasm. Annual review of
679 cell and developmental biology. 2007;23:23-43.

680 6. Staring J, Raaben M, Brummelkamp TR. Viral escape from endosomes and host
681 detection at a glance. J Cell Sci. 2018;131(15).

682 7. Harrison SC. Viral membrane fusion. Virology. 2015;479-480:498-507.

683 8. White JM, Whittaker GR. Fusion of Enveloped Viruses in Endosomes. Traffic.
684 2016;17(6):593-614.

685 9. Sieczkarski SB, Whittaker GR. Viral entry. Current topics in microbiology and
686 immunology. 2005;285:1-23.

687 10. Plemper RK. Cell entry of enveloped viruses. Current opinion in virology.
688 2011;1(2):92-100.

689 11. Stewart PL, Dermody TS, Nemerow GR. Structural basis of nonenveloped virus
690 cell entry. Advances in protein chemistry. 2003;64:455-91.

691 12. Kumar CS, Dey D, Ghosh S, Banerjee M. Breach: Host Membrane Penetration
692 and Entry by Nonenveloped Viruses. Trends Microbiol. 2018;26(6):525-37.

693 13. Banerjee M, Johnson JE. Activation, exposure and penetration of virally
694 encoded, membrane-active polypeptides during non-enveloped virus entry. Curr Protein
695 Pept Sci. 2008;9(1):16-27.

696 14. Bouziat R, Hinterleitner R, Brown JJ, Stencel-Baerenwald JE, Ikizler M, Mayassi
697 T, et al. Reovirus infection triggers inflammatory responses to dietary antigens and
698 development of celiac disease. Science. 2017;356(6333):44-50.

699 15. Dryden KA, Wang G, Yeager M, Nibert ML, Coombs KM, Furlong DB, et al. Early
700 steps in reovirus infection are associated with dramatic changes in supramolecular
701 structure and protein conformation: analysis of virions and subviral particles by
702 cryoelectron microscopy and image reconstruction. J Cell Biol. 1993;122(5):1023-41.

703 16. Zhang X, Ji Y, Zhang L, Harrison SC, Marinescu DC, Nibert ML, et al. Features
704 of reovirus outer capsid protein m1 revealed by electron cryomicroscopy and image
705 reconstruction of the virion at 7.0 Å resolution. Structure. 2005;13(10):1545-57.

17. Dermody TS, Parker JS, Sherry B. Orthoreoviruses. In: Knipe DM, Howley PM, editors. Fields Virology. 2. 6th ed. Philadelphia: Lippincott Williams & Wilkins; 2013. p. 1304-46.

18. Gummersheimer SL, Snyder AJ, Danthi P. Control of capsid transformations during reovirus entry. Viruses. 2021;13(2):153.

19. Roth AN, Aravamudhan P, Fernández de Castro I, Tenorio R, Risco C, Dermody TS. Ins and outs of reovirus: vesicular trafficking in viral entry and egress. Trends Microbiol. 2021;29(4):363-75.

20. Borsa J, Sargent MD, Lievaart PA, Copps TP. Reovirus: evidence for a second step in the intracellular uncoating and transcriptase activation process. Virology. 1981;111(1):191-200.

21. Sturzenbecker LJ, Nibert ML, Furlong DB, Fields BN. Intracellular digestion of reovirus particles requires a low pH and is an essential step in the viral infectious cycle. J Virol 1987;61(8):2351-61.

22. Ebert DH, Deussing J, Peters C, Dermody TS. Cathepsin L and cathepsin B mediate reovirus disassembly in murine fibroblast cells. J Biol Chem. 2002;277(27):24609-17.

23. Baer GS, Dermody TS. Mutations in reovirus outer-capsid protein s3 selected during persistent infections of L cells confer resistance to protease inhibitor E64. J Virol. 1997;71:4921-8.

24. Silverstein SC, Astell C, Levin DH, Schonberg M, Acs G. The mechanism of reovirus uncoating and gene activation in vivo. Virology. 1972;47(3):797-806.

25. Snyder AJ, Danthi P. Lipid membranes facilitate conformational changes required for reovirus cell entry. J Virol. 2015;90(5):2628-38.

26. Snyder AJ, Danthi P. Lipids cooperate with the reovirus membrane penetration peptide to facilitate particle uncoating. J Biol Chem. 2016;291(52):26773-85.

27. Odegard AL, Chandran K, Zhang X, Parker JS, Baker TS, Nibert ML. Putative autocleavage of outer capsid protein m1, allowing release of myristoylated peptide m1N during particle uncoating, is critical for cell entry by reovirus. J Virol. 2004;78(16):8732-45.

28. Agosto MA, Ivanovic T, Nibert ML. Mammalian reovirus, a nonfusogenic nonenveloped virus, forms size-selective pores in a model membrane. Proc Natl Acad Sci U S A. 2006;103(44):16496-501.

29. Ivanovic T, Agosto MA, Zhang L, Chandran K, Harrison SC, Nibert ML. Peptides released from reovirus outer capsid form membrane pores that recruit virus particles. EMBO J. 2008;27(8):1289-98.

30. Chandran K, Farsetta DL, Nibert ML. Strategy for nonenveloped virus entry: a hydrophobic conformer of the reovirus membrane penetration protein m1 mediates membrane disruption. J Virol. 2002;76(19):9920-33.

745 31. Zhang L, Agosto MA, Ivanovic T, King DS, Nibert ML, Harrison SC.
746 Requirements for the formation of membrane pores by the reovirus myristoylated
747 micro1N peptide. J Virol. 2009;83(14):7004-14.

748 32. Carstea ED, Morris JA, Coleman KG, Loftus SK, Zhang D, Cummings C, et al.
749 Niemann-Pick C1 disease gene: homology to mediators of cholesterol homeostasis.
750 Science. 1997;277(5323):228-31.

751 33. Ioannou YA. The structure and function of the Niemann-Pick C1 protein.
752 Molecular genetics and metabolism. 2000;71(1-2):175-81.

753 34. Kwon HJ, Abi-Mosleh L, Wang ML, Deisenhofer J, Goldstein JL, Brown MS, et
754 al. Structure of N-terminal domain of NPC1 reveals distinct subdomains for binding and
755 transfer of cholesterol. Cell. 2009;137(7):1213-24.

756 35. Konopka-Anstadt JL, Mainou BA, Sutherland DM, Sekine Y, Strittmatter SM,
757 Dermody TS. The Nogo receptor NgR1 mediates infection by mammalian reovirus. Cell
758 Host Microbe. 2014;15(6):681-91.

759 36. Barton ES, Connolly JL, Forrest JC, Chappell JD, Dermody TS. Utilization of
760 sialic acid as a coreceptor enhances reovirus attachment by multistep adhesion
761 strengthening. J Biol Chem. 2001;276(3):2200-11.

762 37. Urbanek K, Sutherland DM, Orchard RC, Wilen CB, Knowlton JJ, Aravamudhan
763 P, et al. Cytidine monophosphate N-acetylneuraminic acid synthetase and solute carrier
764 family 35 member A1 are required for reovirus binding and infection. J Virol. 2020;95(2).

765 38. Gentsch JR, Pacitti AF. Effect of neuraminidase treatment of cells and effect of
766 soluble glycoproteins on type 3 reovirus attachment to murine L cells. J Virol.
767 1985;56(2):356-64.

768 39. Avula K, Singh B, Kumar PV, Syed GH. Role of Lipid Transfer Proteins (LTPs) in
769 the Viral Life Cycle. Frontiers in microbiology. 2021;12:673509.

770 40. Lai CM, Mainou BA, Kim KS, Dermody TS. Directional release of reovirus from
771 the apical surface of polarized endothelial cells. mBio. 2013;4(2):e00049-13.

772 41. Fu J, Li L, Huo D, Zhi S, Yang R, Yang B, et al. Astrocyte-Derived TGFβ1
773 Facilitates Blood-Brain Barrier Function via Non-Canonical Hedgehog Signaling in Brain
774 Microvascular Endothelial Cells. Brain Sci. 2021;11(1).

775 42. Borsa J, Copps TP, Sargent MD, Long DG, Chapman JD. New intermediate
776 subviral particles in the in vitro uncoating of reovirus virions by chymotrypsin. J Virol.
777 1973;11(4):552-64.

778 43. Parker JS, Broering TJ, Kim J, Higgins DE, Nibert ML. Reovirus core protein m2
779 determines the filamentous morphology of viral inclusion bodies by interacting with and
780 stabilizing microtubules. J Virol. 2002;76(9):4483-96.

781 44. Aravamudhan P, Raghunathan K, Konopka-Anstadt J, Pathak A, Sutherland DM,
782 Carter BD, et al. Reovirus uses macropinocytosis-mediated entry and fast axonal
783 transport to infect neurons. PLoS Pathog. 2020;16(2):e1008380.

784 45. Elrick MJ, Yu T, Chung C, Lieberman AP. Impaired proteolysis underlies
785 autophagic dysfunction in Niemann-Pick type C disease. Human molecular genetics.
786 2012;21(22):4876-87.

787 46. Carette JE, Raaben M, Wong AC, Herbert AS, Obernosterer G, Mulherkar N, et
788 al. Ebola virus entry requires the cholesterol transporter Niemann-Pick C1. Nature.
789 2011;477(7364):340-3.

790 47. Miller EH, Obernosterer G, Raaben M, Herbert AS, Deffieu MS, Krishnan A, et al.
791 Ebola virus entry requires the host-programmed recognition of an intracellular receptor.
792 EMBO J. 2012;31(8):1947-60.

793 48. Rosenbaum AI, Zhang G, Warren JD, Maxfield FR. Endocytosis of beta-
794 cyclodextrins is responsible for cholesterol reduction in Niemann-Pick type C mutant
795 cells. Proc Natl Acad Sci U S A. 2010;107(12):5477-82.

796 49. Peake KB, Vance JE. Normalization of cholesterol homeostasis by 2-
797 hydroxypropyl-β-cyclodextrin in neurons and glia from Niemann-Pick C1 (NPC1)-
798 deficient mice. J Biol Chem. 2012;287(12):9290-8.

799 50. Liu B, Turley SD, Burns DK, Miller AM, Repa JJ, Dietschy JM. Reversal of
800 defective lysosomal transport in NPC disease ameliorates liver dysfunction and
801 neurodegeneration in the npc1-/- mouse. Proc Natl Acad Sci U S A. 2009;106(7):2377-
802 82.

803 51. Ory DS, Ottinger EA, Farhat NY, King KA, Jiang X, Weissfeld L, et al. Intrathecal
804 2-hydroxypropyl-β-cyclodextrin decreases neurological disease progression in
805 Niemann-Pick disease, type C1: a non-randomised, open-label, phase 1-2 trial. Lancet.
806 2017;390(10104):1758-68.

807 52. Poh MK, Shui G, Xie X, Shi PY, Wenk MR, Gu F. U18666A, an intra-cellular
808 cholesterol transport inhibitor, inhibits dengue virus entry and replication. Antiviral
809 research. 2012;93(1):191-8.

810 53. Cuesta-Geijo M, Chiappi M, Galindo I, Barrado-Gil L, Muñoz-Moreno R,
811 Carrascosa JL, et al. Cholesterol Flux Is Required for Endosomal Progression of
812 African Swine Fever Virions during the Initial Establishment of Infection. J Virol.
813 2016;90(3):1534-43.

814 54. Elgner F, Ren H, Medvedev R, Ploen D, Himmelsbach K, Boller K, et al. The
815 Intracellular Cholesterol Transport Inhibitor U18666A Inhibits the Exosome-Dependent
816 Release of Mature Hepatitis C Virus. J Virol. 2016;90(24):11181-96.

817 55. Yin X, Ambardekar C, Lu Y, Feng Z. Distinct Entry Mechanisms for
818 Nonenveloped and Quasi-Enveloped Hepatitis E Viruses. J Virol. 2016;90(8):4232-42.

819 56. Rivera-Serrano EE, González-López O, Das A, Lemon SM. Cellular entry and
820 uncoating of naked and quasi-enveloped human hepatoviruses. eLife. 2019;8.

821 57. Sobo K, Le Blanc I, Luyet PP, Fivaz M, Ferguson C, Parton RG, et al. Late
822 endosomal cholesterol accumulation leads to impaired intra-endosomal trafficking. PloS
823 one. 2007;2(9):e851.

824 58. Vanier MT. Niemann-Pick disease type C. Orphanet J Rare Dis. 2010;5:16.

825 59. Koller D, Lohner K. The role of spontaneous lipid curvature in the interaction of
826 interfacially active peptides with membranes. Biochimica et biophysica acta.
827 2014;1838(9):2250-9.

828 60. Maier O, Galan DL, Wodrich H, Wiethoff CM. An N-terminal domain of
829 adenovirus protein VI fragments membranes by inducing positive membrane curvature.
830 Virology. 2010;402(1):11-9.

831 61. Guo X, Steinkühler J, Marin M, Li X, Lu W, Dimova R, et al. Interferon-Induced
832 Transmembrane Protein 3 Blocks Fusion of Diverse Enveloped Viruses by Altering
833 Mechanical Properties of Cell Membranes. ACS Nano. 2021;15(5):8155-70.

834 62. Anafu AA, Bowen CH, Chin CR, Brass AL, Holm GH. Interferon-inducible
835 transmembrane protein 3 (IFITM3) restricts reovirus cell entry. J Biol Chem.
836 2013;288(24):17261-71.

837 63. Moyer CL, Wiethoff CM, Maier O, Smith JG, Nemerow GR. Functional genetic
838 and biophysical analyses of membrane disruption by human adenovirus. J Virol.
839 2011;85(6):2631-41.

840 64. Patel A, Mohl BP, Roy P. Entry of Bluetongue Virus Capsid Requires the Late
841 Endosome-specific Lipid Lysobisphosphatidic Acid. J Biol Chem. 2016;291(23):12408-
842 19.

843 65. Silva-Ayala D, López T, Gutiérrez M, Perrimon N, López S, Arias CF. Genome-
844 wide RNAi screen reveals a role for the ESCRT complex in rotavirus cell entry. Proc
845 Natl Acad Sci U S A. 2013;110(25):10270-5.

846 66. Snyder A, Abad A, Danthi, P. A CRISPR-Cas9 screen reveals a role for WD
847 repeat-containing protein (WDR81) in the entry of late penetrating viruses.
848 2021 https://biorxiv.org/cgi/content/short/2021.09.26.461887v1

849 67. Liu K, Jian Y, Sun X, Yang C, Gao Z, Zhang Z, et al. Negative regulation of
850 phosphatidylinositol 3-phosphate levels in early-to-late endosome conversion. J Cell
851 Biol. 2016;212(2):181-98.

852 68. Wheeler S, Schmid R, Sillence DJ. Lipid⁻Protein Interactions in Niemann⁻Pick
853 Type C Disease: Insights from Molecular Modeling. Int J Mol Sci. 2019;20(3).

854 69. Rentero C, Blanco-Munoz P, Meneses-Salas E, Grewal T, Enrich C. Annexins-
855 coordinators of cholesterol homeostasis in endocytic pathways. Int J Mol Sci.
856 2018;19(5):E1444.

857 70. de Diego I, Schwartz F, Siegfried H, Dauterstedt P, Heeren J, Beisiegel U, et al.
858 Cholesterol modulates the membrane binding and intracellular distribution of annexin 6.
859 J Biol Chem. 2002;277(35):32187-94.

860 71. Mayran N, Parton RG, Gruenberg J. Annexin II regulates multivesicular
861 endosome biogenesis in the degradation pathway of animal cells. EMBO J.
862 2003;22(13):3242-53.

863 72. Hirsch AJ. The use of RNAi-based screens to identify host proteins involved in
864 viral replication. Future Microbiol. 2010;5(2):303-11.

865 73. Puschnik AS, Majzoub K, Ooi YS, Carette JE. A CRISPR toolbox to study virus-
866 host interactions. Nat Rev Microbiol. 2017;15(6):351-64.

867 74. Furlong DB, Nibert ML, Fields BN. Sigma 1 protein of mammalian reoviruses
868 extends from the surfaces of viral particles. J Virol. 1988;62(1):246-56.

869 75. Virgin HW, Bassel-Duby R, Fields BN, Tyler KL. Antibody protects against lethal
870 infection with the neurally spreading reovirus type 3 (Dearing). J Virol.
871 1988;62(12):4594-604.

872 76. Smith RE, Zweerink HJ, Joklik WK. Polypeptide components of virions, top
873 component and cores of reovirus type 3. Virology. 1969;39(4):791-810.

874 77. Fecek RJ, Busch R, Lin H, Pal K, Cunningham CA, Cuff CF. Production of Alexa
875 Fluor 488-labeled reovirus and characterization of target cell binding, competence, and
876 immunogenicity of labeled virions. Journal of immunological methods. 2006;314(1-
877 2):30-7.

878 78. Wetzel JD, Chappell JD, Fogo AB, Dermody TS. Efficiency of viral entry
879 determines the capacity of murine erythroleukemia cells to support persistent infections
880 by mammalian reoviruses. J Virol. 1997;71(1):299-306.

881 79. Chandran K, Walker SB, Chen Y, Contreras CM, Schiff LA, Baker TS, et al. In
882 vitro recoating of reovirus cores with baculovirus-expressed outer-capsid proteins m1
883 and s3. J Virol. 1999;73(5):3941-50.

884 80. Orchard RC, Wilen CB, Doench JG, Baldridge MT, McCune BT, Lee YC, et al.
885 Discovery of a proteinaceous cellular receptor for a norovirus. Science.
886 2016;353(6302):933-6.

887 81. Doench JG, Fusi N, Sullender M, Hegde M, Vaimberg EW, Donovan KF, et al.
888 Optimized sgRNA design to maximize activity and minimize off-target effects of
889 CRISPR-Cas9. Nat Biotechnol. 2016;34(2):184-91.

890 82. Spence JS, Krause TB, Mittler E, Jangra RK, Chandran K. Direct visualization of
891 ebola virus fusion triggering in the endocytic pathway. mBio. 2016;7(1):e01857-15.

892 83. Dehairs J, Talebi A, Cherifi Y, Swinnen JV. CRISP-ID: decoding CRISPR
893 mediated indels by Sanger sequencing. Sci Rep. 2016;6:28973.

894 84. Olivio-Marin JC. Extraction of spots in biological images using multi-scale
895 products. Pattern Recognition. 2002;35(9):1989-96.

896

FIGURE LEGENDS

FIG 1 CRISPR and siRNA screens identify NPC1 as a cellular factor required for reovirus infection. (A) The top 20 candidates from the CRISPR screen using reovirus strains T1L and T3D are ranked by their STAR scores. Heat map indicates STAR values. (B) Genes from the siRNA screen using reovirus strain T3SA+ common to the CRISPR screen using T1L and T3D, excluding ribosomal genes. Heat map indicates z-score values. (C) Venn diagram of genes from the CRISPR screens using T1L and T3D and the siRNA screen using T3SA+. (D) Molecular function pathways using Gene Ontology to analyze genes from the CRISPR screen common to T1L and T3D. (E) KEGG pathways identified for the CRISPR screen using T1L (red) and T3D (blue) and siRNA screen using T3SA+ (light blue).

FIG 2 Viral infectivity and titers following adsorption by reovirus virions and ISVPs. (A, B) WT, KO, and KO+ HBMECs were adsorbed with reovirus (A) virions or (B) ISVPs at MOIs of 10,000 or 100 particles/cell, respectively, and fixed at 18 h post-adsorption. The percentage of infected cells was determined by enumerating reovirus-infected cells following immunostaining with a reovirus-specific antiserum. (C-F) WT, KO, and KO+ cells were adsorbed with reovirus (C, E) virions at an MOI of 1 PFU/cell or (D, F) ISVPs at an MOI of 5 particles/cell. Viral titers in cell-culture supernatants and lysates were determined by plaque assay at 0, 24, and 48 h post-adsorption. The results are presented as the mean of three independent experiments. Error bars indicated standard deviation. *, $P < 0.05$; **, $P < 0.01$; ***, $P < 0.001$; ****, $P < 0.0001$, as determined by t-test.

922 **FIG 3** Binding, internalization, and uncoating are not disrupted by cholesterol
923 accumulation in NPC1 KO HBMECs. (A) WT, KO, and KO+ HBMECs were adsorbed
924 with Alexa 647 labeled-reovirus virions at an MOI of 10,000 particles/cell at 4°C for 1 h,
925 fixed with 1% PFA, and analyzed for virus binding using flow cytometry. The results are
926 presented as mean virus binding as determined by mean fluorescence intensity (MFI) of
927 three independent experiments. Error bars indicated standard deviation. (B) WT, KO,
928 and KO+ HBMECs were adsorbed with Alexa 647 labeled-reovirus virions at an MOI of
929 10,000 particles/cell at 4°C for 45 min and imaged using high magnification live-cell
930 imaging, with images captured every ~ 25 seconds. Representative micrographs from
931 videos at the indicated intervals are shown. Scale bars, 10 μm. (C) WT, KO, and KO+
932 HBMECs were adsorbed with reovirus virions at an MOI of 10,000 particles/cell at 4°C
933 for 1 h and lysed at the intervals post-adsorption shown. Cell lysates were subjected to
934 electrophoresis and immunoblotting using a reovirus-specific polyclonal rabbit
935 antiserum. The results are presented as the mean ratio of the δ and μ1C bands from
936 three independent experiments. Error bars indicate standard deviation. Differences are
937 not significant, as determined by two-tailed unpaired t-test.
938
939 **FIG 4** Cytosolic entry of reovirus cores. (A) WT, KO, and KO+ HBMECs were adsorbed
940 with Alexa 647 labeled-reovirus virions at an MOI of 10,000 particles/cell at 37°C for 45
941 min and fixed with 4% PFA at 8 h post-adsorption. Cells were stained with DAPI, a CD-
942 63-specific antibody to label endosomes, and an antiserum specific for reovirus cores,
943 and imaged using confocal microscopy. Representative confocal micrographs are
944 shown. (B) Colocalization of reovirus, cores, and endosomes was analyzed using the
945 JaCoP plugin function from ImageJ. The results are presented as the mean
946 colocalization (quantified by Manders coefficient) of ~ 50 cells from three independent

947 experiments. Error bars indicate standard deviation. **, $P < 0.01$; ***, $P < 0.001$, as
948 determined by two-tailed unpaired t-test.
949
950 **FIG 5** Synthesis of nascent RNA is reduced in NPC1 KO HBMECs. WT, KO, and KO+
951 HBMECs were adsorbed with reovirus virions at an MOI of 1 PFU/cell at 37°C for 1 h,
952 lysed at the intervals post-adsorption shown, and assayed for positive-sense reovirus
953 s4 RNA by RT-qPCR. The results are presented as the mean number of copies of
954 reovirus s4 RNA by qPCR from two independent experiments. Error bars indicate
955 standard errors of the mean. **, $P < 0.01$; ***, $P < 0.001$, as determined by t-test.
956
957 **FIG 6** HβCD treatment restores reovirus infection of NPC1 KO HBMECs. WT, KO, and
958 KO+ HBMECs were pretreated with 1 mM HβCD or PBS for 24 h, adsorbed with
959 reovirus virions or ISVPs at MOIs of 10,000 or 100 particles/cell, respectively, and fixed
960 at 18 h post-adsorption. The percentage of infected cells was determined by
961 enumerating reovirus-infected cells following immunostaining with a reovirus-specific
962 antiserum. The results are presented as the mean of three independent experiments.
963 Error bars indicated standard deviation. ***, $P < 0.001$ as determined by two-tailed
964 unpaired t-test.
965
966 **SUPPLEMENTAL MATERIALS**
967 **FIGURES AND MOVIES**
968
969 **FIG S1** Effect on cholesterol distribution by disruption of NPC1 expression. (A, B)
970 Lysates of WT, KO, and KO+ HBMECs were subjected to electrophoresis and
971 immunoblotting using an NPC1 antiserum. GAPDH was used as loading control. A

representative immunoblot is shown. The results are presented as the mean of two independent experiments. Error bars indicate standard deviation. Statistical analysis was done by two-tailed unpaired t-test. (C) WT, KO, and KO+ HBMECs were stained with filipin III to detect cholesterol distribution. Representative images are shown. Scale bars, 10 μm. (D) WT, KO, and KO+ HBMECs were stained with filipin III and an anti-CD63 antibody to detect the subcellular localization of cholesterol. Representative images are shown. Scale bars, 10 μm.

FIG S2 Viral infectivity following adsorption by T1L, T3D, and T3SA+ virions. (A, B) WT, KO, and KO+ HBMECs were adsorbed with reovirus virions at MOIs of 10,000 particles/cell, and fixed at 18 h post-adsorption. The percentage of infected cells was determined by enumerating reovirus-infected cells following immunostaining with a reovirus-specific antiserum. Error bars indicated standard deviation. **, $P < 0.01$; ***, $P < 0.001$, as determine by 2 way ANOVA, Tukey's multiple comparisons test.

FIG S3 HβCD treatment restores cholesterol efflux in KO cells. (A) WT, KO, and KO+ HBMECs were treated with HβCD at the concentrations shown for 48 h and assessed for viability using the Presto blue cell viability reagent. The results are presented as the mean cell viability of three independent experiments. Error bars indicated standard deviation. **, $P < 0.01$; ***, $P < 0.001$; ****, $P < 0.0001$, as determined by two-way ANOVA. (B, C) Cells were treated with 1 mM HβCD or PBS (mock) for 48 h, fixed with 4% PFA, stained with filipin III, and imaged using confocal microscopy. (B) The results are presented as the mean filipin III staining (quantified by MFI) of ~ 50 cells from three independent experiments. Error bars indicate the minimum and the maximum values. *, $P < 0.05$; ****, $P < 0.0001$, as determined by two-tailed unpaired t-test. (C) Representative images of cholesterol distribution in HβCD-treated and mock-treated cells are shown. Scale bars, 10 μm.

997

998 **VIDEO 1, 2, and 3** High-magnification, live-cell microscopy of fluorescent reovirus virion
999 transport in WT, KO, and KO+ HBMECs. (1) WT, (2) KO, and (3) KO+ cells were
1000 adsorbed with Alexa 647-labeled reovirus virions at an MOI of 10,000 particles/cell at
1001 4°C for 45 min. Fluorescence and brightfield images were captured every ~ 25 seconds
1002 for 36 min.

1003

1004 **VIDEO 4, 5, and 6** Tracking of fluorescent reovirus virions recruited to a perinuclear
1005 region following entry. Trajectories of reovirus virions during internalization into WT, KO,
1006 and KO+ HBMECs from videos 1, 2, and 3 were tracked with the spot-tracking plugin
1007 function of Icy-Bioimage analysis software (84). Cell contour was defined as a region of
1008 interest (ROI), and ~ 7 pixels/spot were monitored. The colored bar represents the
1009 trajectory depending on time, in which each color (from yellow to red) corresponds to an
1010 interval of ~ 7.5 min in the time-lapse videos. Scale bars, 10 μm.

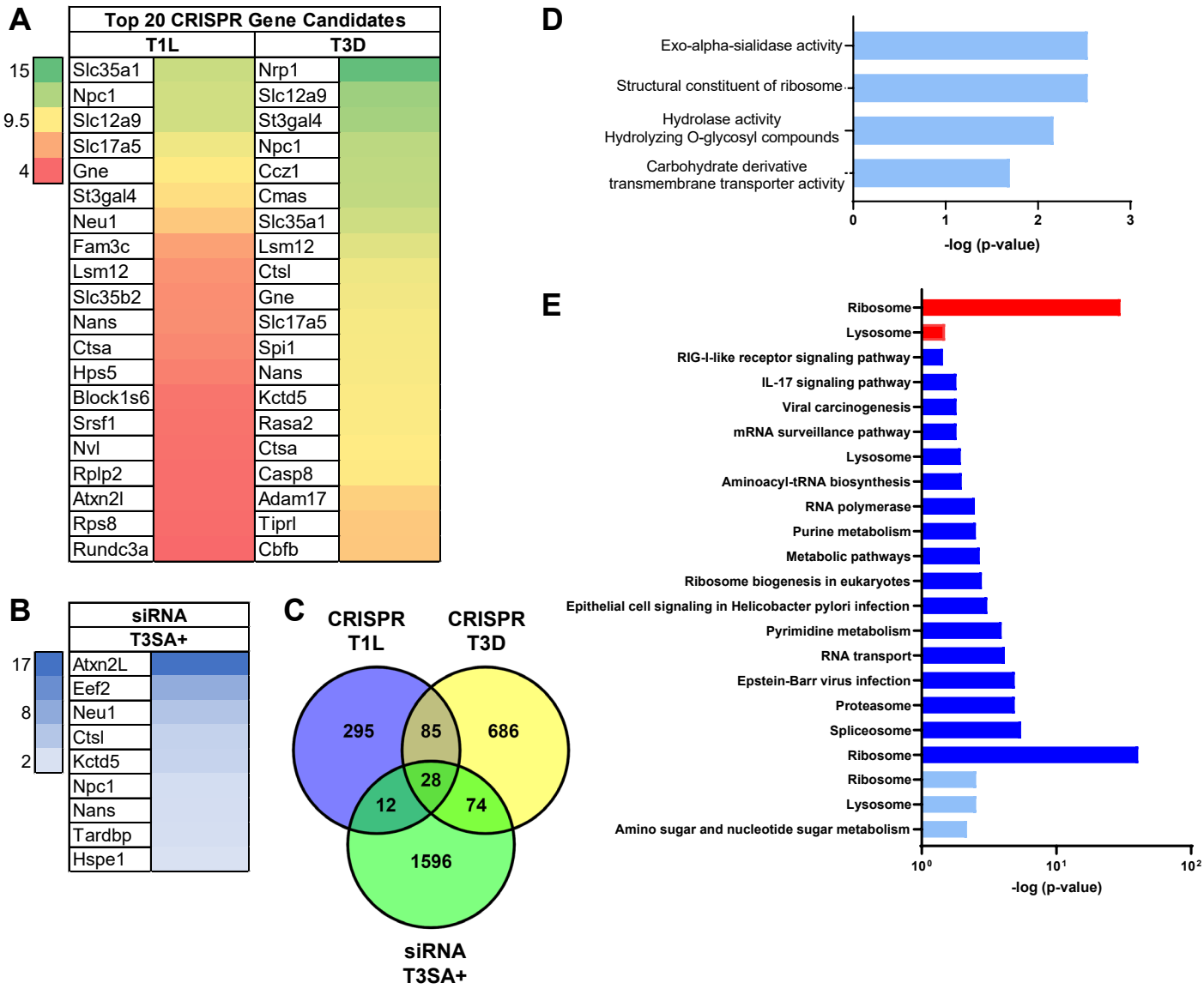

FIG 1 CRISPR and siRNA screens identify NPC1 as a cellular factor required for reovirus infection. (A) The top 20 candidates from the CRISPR screen using reovirus strains T1L and T3D are ranked by their STAR scores. Heat map indicates STAR values. (B) Genes from the siRNA screen using reovirus strain T3SA+ common to the CRISPR screen using T1L and T3D, excluding ribosomal genes. Heat map indicates z-score values. (C) Venn diagram of genes from the CRISPR screens using T1L and T3D and the siRNA screen using T3SA+. (D) Molecular function pathways using Gene Ontology to analyze genes from the CRISPR screen common to T1L and T3D. (E) KEGG pathways identified for the CRISPR screen using T1L (red) and T3D (blue) and siRNA screen using T3SA+ (light blue).

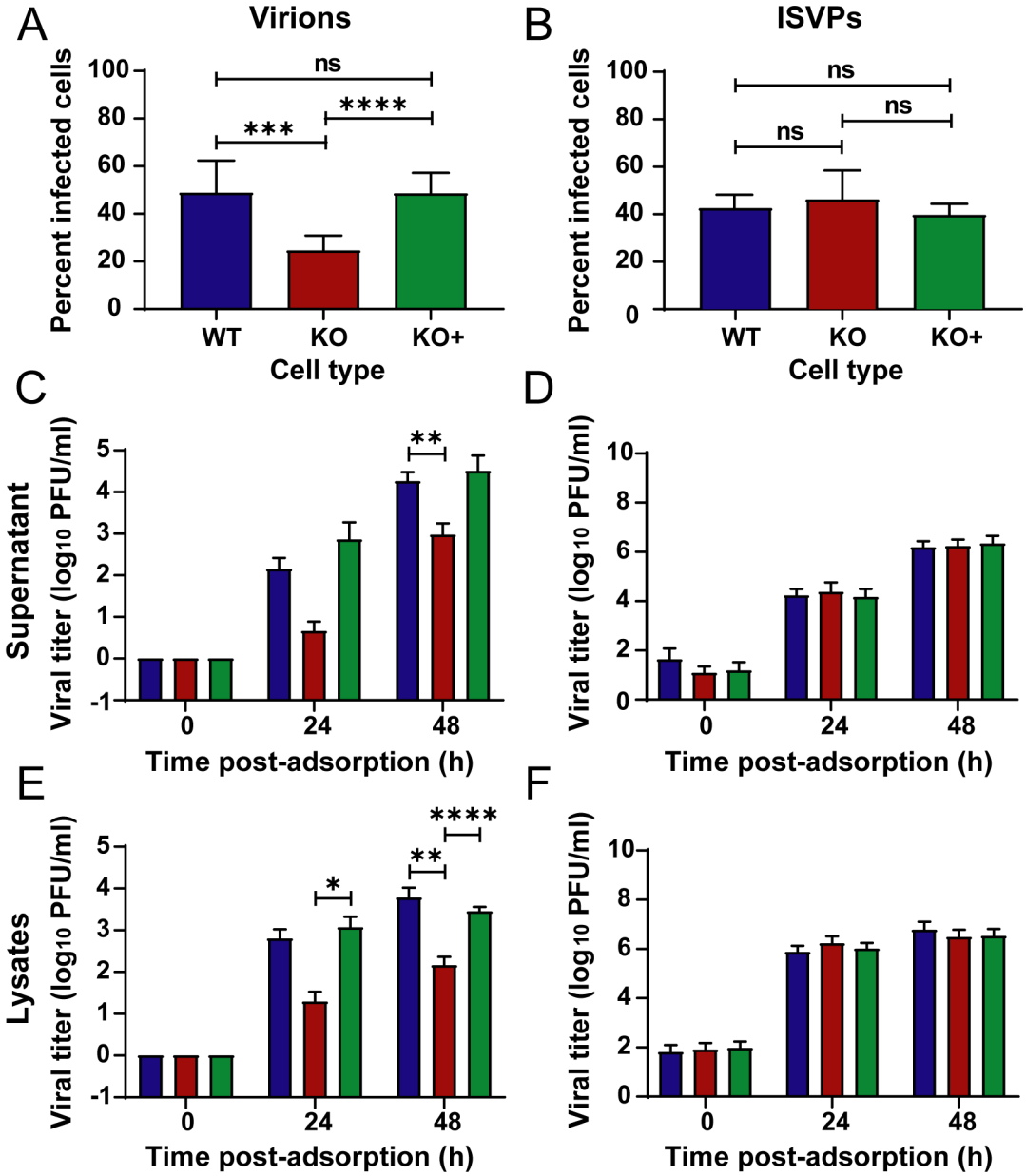

FIG 2 Viral infectivity and titers following adsorption by reovirus virions and ISVPs. (A, B) WT, KO, and KO+ HBMECs were adsorbed with reovirus (A) virions or (B) ISVPs at MOIs of 10,000 or 100 particles/cell, respectively, and fixed at 18 h post-adsorption. The percentage of infected cells was determined by enumerating reovirus-infected cells following immunostaining with a reovirus-specific antiserum. (C-F) WT, KO, and KO+ cells were adsorbed with reovirus (C, E) virions at an MOI of 1 PFU/cell or (D, F) ISVPs at an MOI of 5 particles/cell. Viral titers in cell-culture supernatants and lysates were determined by plaque assay at 0, 24, and 48 h post-adsorption. The results are presented as the mean of three independent experiments. Error bars indicated standard deviation. *, $P < 0.05$; **, $P < 0.01$; ***, $P < 0.001$; ****, $P < 0.0001$, as determined by t-test.

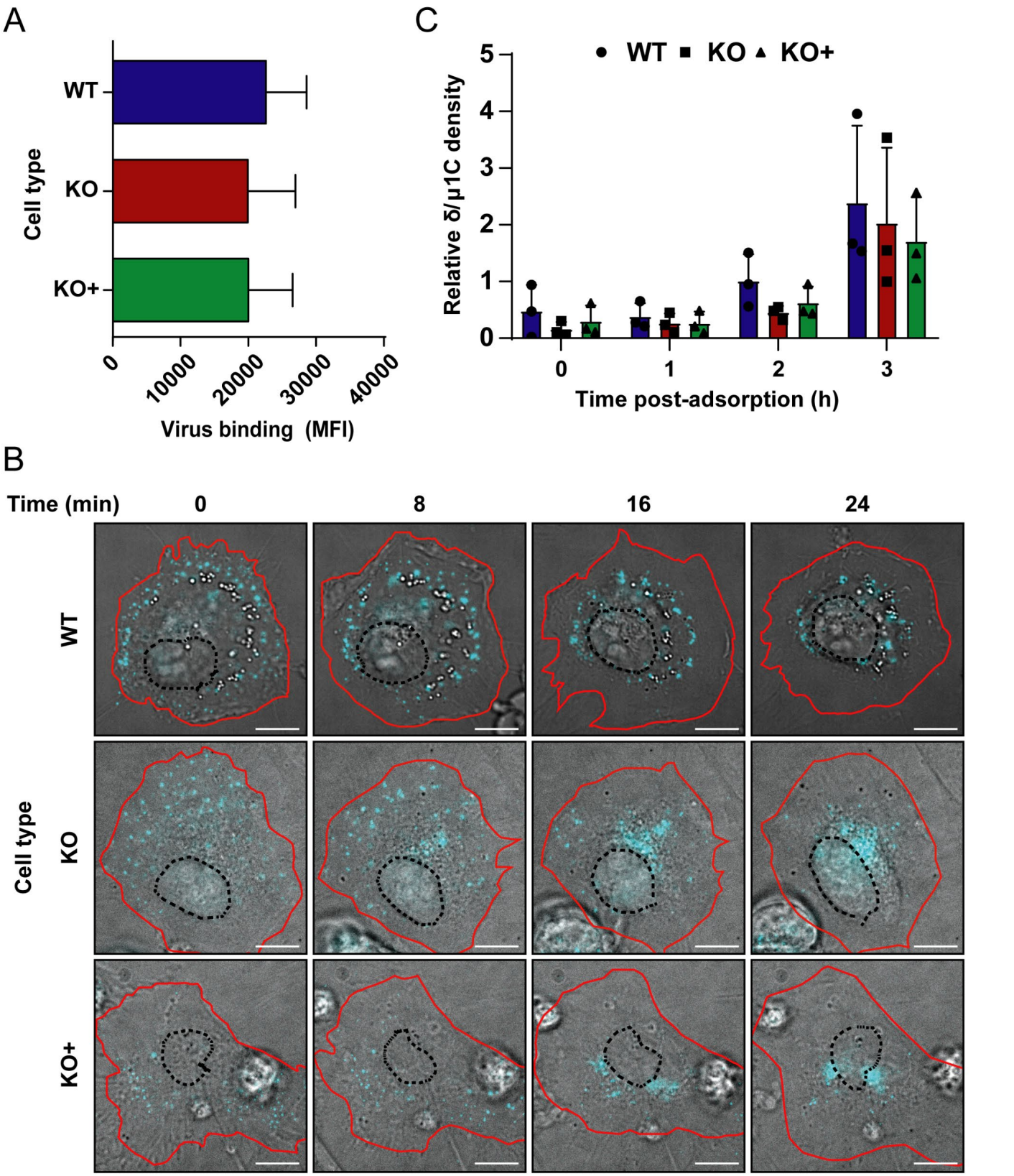

FIG 3 Binding, internalization, and uncoating are not disrupted by cholesterol accumulation in NPC1 KO HBMECs. (A) WT, KO, and KO+ HBMECs were adsorbed with Alexa 647 labeled-reovirus virions at an MOI of 10,000 particles/cell at 4°C for 1 h, fixed with 1% PFA, and analyzed for virus binding using flow cytometry. The results are presented as mean virus binding as determined by mean fluorescence intensity (MFI) of three independent experiments. Error bars indicated standard deviation. (B) WT, KO, and KO+ HBMECs were adsorbed with Alexa 647 labeled-reovirus virions at an MOI of 10,000 particles/cell at 4°C for 45 min and imaged using high magnification live-cell imaging, with images captured every ~ 25 seconds. Representative micrographs from videos at the indicated intervals are shown. Scale bars, 10 µm. (C) WT, KO, and KO+ HBMECs were adsorbed with reovirus virions at an MOI of 10,000 particles/cell at 4°C for 1 h and lysed at the intervals post-adsorption shown. Cell lysates were subjected to electrophoresis and immunoblotting using a reovirus-specific polyclonal rabbit antiserum. The results are presented as the mean ratio of the δ and µ1C bands from three independent experiments. Error bars indicate standard deviation. Differences are not significant, as determined by two-tailed unpaired t-test.

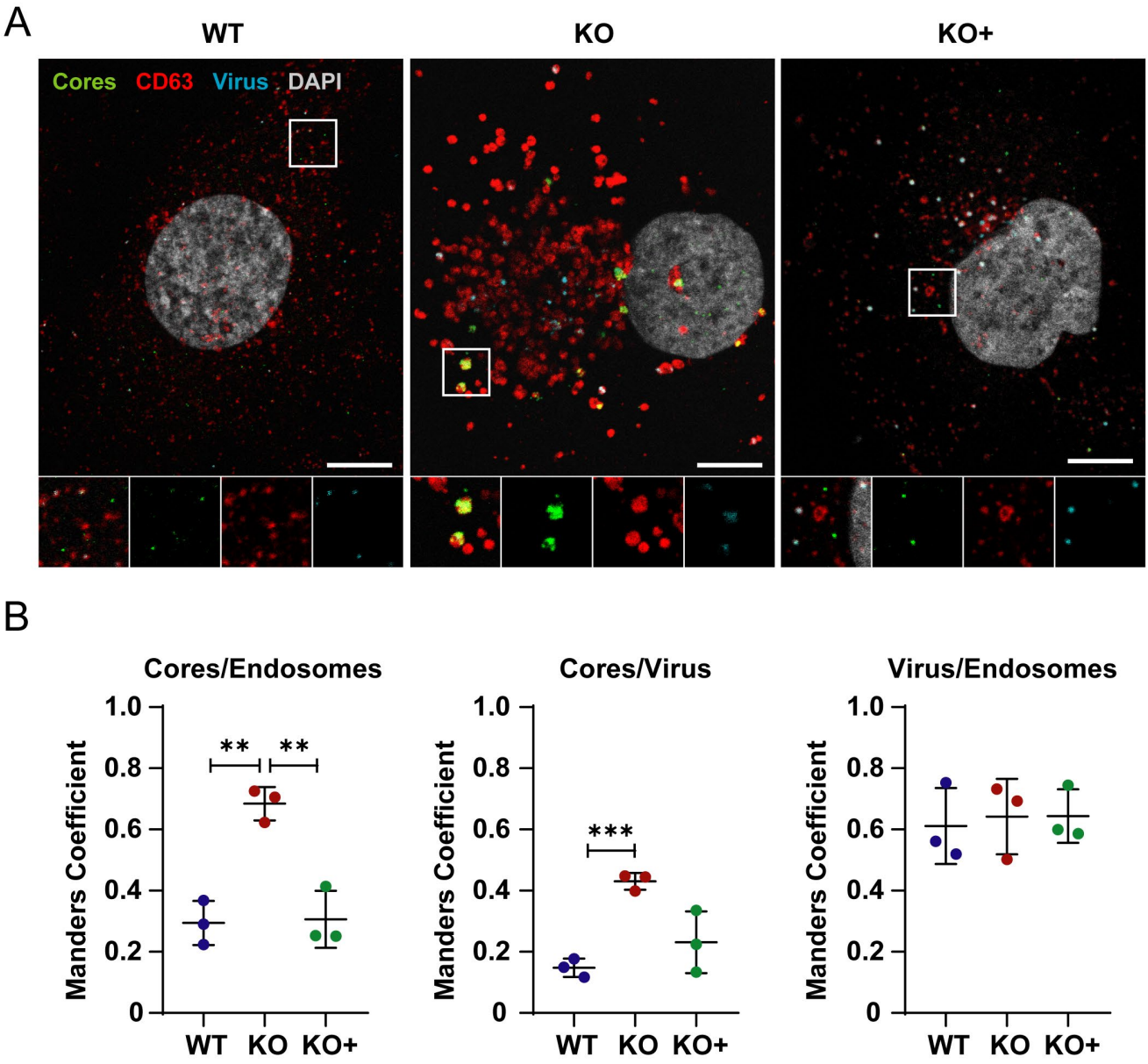

FIG 4 Cytosolic entry of reovirus cores. (A) WT, KO, and KO+ HBMECs were adsorbed with Alexa 647 labeled-reovirus virions at an MOI of 10,000 particles/cell at 37°C for 45 min and fixed with 4% PFA at 8 h post-adsorption. Cells were stained with DAPI, a CD-63-specific antibody to label endosomes, and an antiserum specific for reovirus cores, and imaged using confocal microscopy. Representative confocal micrographs are shown. (B) Colocalization of reovirus, cores, and endosomes was analyzed using the JaCoP plugin function from ImageJ. The results are presented as the mean colocalization (quantified by Manders coefficient) of ~ 50 cells from three independent experiments. Error bars indicate standard deviation. **, $P < 0.01$; ***, $P < 0.001$, as determined by two-tailed unpaired t-test.

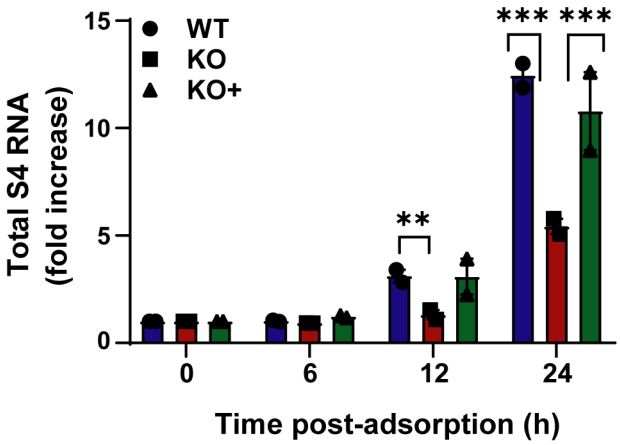

FIG 5 Synthesis of nascent RNA is reduced in NPC1 KO HBMECs. WT, KO, and KO+ HBMECs were adsorbed with reovirus virions at an MOI of 1 PFU/cell at 37°C for 1 h, lysed at the intervals post-adsorption shown, and assayed for positive-sense reovirus s4 RNA by RT-qPCR. The results are presented as the mean number of copies of reovirus s4 RNA by qPCR from two independent experiments. Error bars indicate standard errors of the mean. **, $P < 0.01$; ***, $P < 0.001$, as determined by t-test.

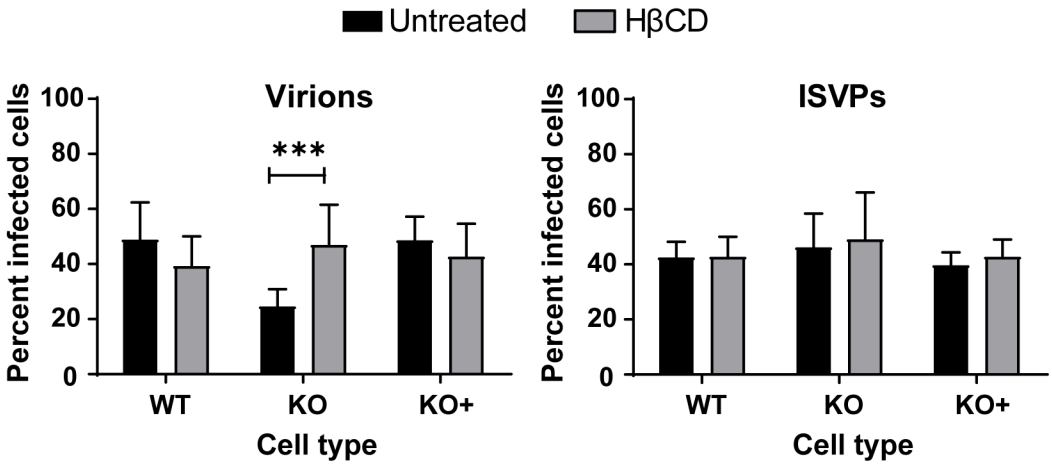

FIG 6 HβCD treatment restores reovirus infection of NPC1 KO HBMECs. WT, KO, and KO+ HBMECs were pretreated with 1 mM HβCD or PBS for 24 h, adsorbed with reovirus virions or ISVPs at MOIs of 10,000 or 100 particles/cell, respectively, and fixed at 18 h post-adsorption. The percentage of infected cells was determined by enumerating reovirus-infected cells following immunostaining with a reovirus-specific antiserum. The results are presented as the mean of three independent experiments. Error bars indicated standard deviation. ***, $P < 0.001$ as determined by two-tailed unpaired t-test.